Effects of Inversion Height and Surface Heat Flux on Downslope Windstorms

CRAIG M. SMITH AND ERIC D. SKYLLINGSTAD

College of Oceanic and Atmospheric Sciences, Oregon State University, Corvallis, Oregon

(Manuscript received 9 September 2010, in final form 24 June 2011)

ABSTRACT

Simulations are presented focusing on the role of temperature inversions in controlling the formation and strength of downslope wind storms. Three mechanisms are examined depending on the relative height of the inversion with respect to the mountain and the stability of vertically propagating mountain waves. For low-level inversions, flows are generated that closely resemble a reduced gravity shallow water hydraulic response with a large vertical displacement of the inversion on the lee side of the mountain. For higher-level inversion cases, simulated flows more closely followed a stratified hydraulic behavior with the inversion acting as a rigid reflective lid. In the third mechanism, downslope winds were forced by a self-induced critical layer located below the inversion height. The presence of the inversion in this case had little effect on the resulting downslope winds.

Observations made on the Falkland Islands show that downslope windstorms may preferentially occur in early morning even without synoptic-scale changes in atmospheric structure. Most windstorms on the Falkland Islands generally have a short jet length; rare, longer jet length storms typically occur in conjunction with a strong low-level inversion. Idealized numerical experiments tend to produce a similar response depending on the presence of strong low-level inversion and surface cooling. Results suggest that surface heating can have significant control on the flow response by reducing the low-level inversion strength, or by changing the stratification and wind velocity below the inversion, thereby preventing a strong downslope windstorm.

1. Introduction

Mechanisms of downslope windstorm formation often vary according to the presence or absence of upstream inversions. In cases with little or no upstream inversion present, internal gravity wave (IGW) breaking can result in the formation of a leeside jet capped by an elevated stagnation zone (Lilly and Zipser 1972; Clark and Peltier 1977; Peltier and Clark 1979; Doyle et al. 2000). When a strong elevated inversion is present the flow can behave more like a subcritical to supercritical transition of the reduced gravity shallow water (RGSW) mode (Long 1954; Gohm et al. 2008; Flamant et al. 2002; Drobinski et al. 2001). The dichotomy between these two mechanisms for downslope windstorm formation, however, is somewhat ambiguous. A major distinction between these two models is that continuously stratified fluids allow for vertical energy propagation, which in some circumstances can be constrained through the creation of a self-induced critical layer via IGW breaking, whereas the RGSW mechanism does not require stratification anywhere besides the inversion itself. In fact, stratification in the RGSW case can act to decrease the strength of downslope flows by transporting momentum via vertical wave propagation.

If vertically propagating waves are reflected from either a strong change in stratification (inversion) or a rigid lid (e.g., as in the ocean), then a third mechanism for downwind storm formation is possible. In this case the stratified flow separates from a dividing streamline at the reflection level and behaves much like a transcritical RGSW case, but without a fluid interfacial boundary. The dynamics of this hybrid situation are presented in Smith (1985) and are very similar to classic limited depth results presented by Long (1955) and more recently Lamb (1994). The dynamics of these downslope windstorms, whose mechanism does not clearly fall into IGW breaking or the RGSW transition, have not been thoroughly explored, especially considering that the criteria for their formation may be substantially different than the criteria for IGW breaking in a continuously stratified system.

Previous studies have suggested this ambiguity in the Alps, where the foehn sometimes occurs with IGW breaking as shown by lidar observations (Gohm and

Corresponding author address: Craig Smith, COAS, Oregon State University, 104 COAS Admin. Bldg., Corvallis, OR 97331.
E-mail: csmith@coas.oregonstate.edu

DOI: 10.1175/2011MWR3619.1

Mayr 2004), and also occurs during periods in which upstream inversions are observed. Upstream inversions are also noted with the bora, while at other times IGW breaking is the dominant wind acceleration mechanism (Glasnovic and Jurcec 1990; Klemp and Durran 1987; Gohm and Mayr 2005; Belusic et al. 2007; Klemp et al. 1997; Gohm et al. 2008). Recent observations on the Falkland Islands (Mobbs et al. 2005) illustrate the overlapping mechanisms even more clearly. In some cases the authors show that downslope windstorms are correlated with nondimensional mountain height,

$$\hat{h} = \frac{Nh}{\upsilon}, \tag{1}$$

where N is the Brunt–Väisälä frequency,

$$N = \sqrt{\frac{g}{\theta_0}\frac{\partial\theta}{\partial z}}, \tag{2}$$

h is the ridge height, υ is the cross-ridge velocity, g is the acceleration due to gravity, θ is the potential temperature, and θ_0 is a reference potential temperature, suggesting that IGW nonlinearity and breaking is the dominant mechanism for the downslope windstorms. At other times, the authors show that the lee-slope winds are better explained using a shallow water Froude number based on an inversion height,

$$\mathrm{Fr} = \frac{\upsilon}{\sqrt{g' z_i}}, \tag{3}$$

where the reduced gravity, g' is defined as

$$g' = g\frac{\Delta\theta}{\theta_0}, \tag{4}$$

z_i is the height of the inversion, and $\Delta\theta$ is the strength of the inversion. The Froude number is the ratio of fluid speed to the speed of RGSW waves, and indicates the direction of propagation for trapped barotropic interfacial waves on the inversion.

To adequately address and differentiate the role of upstream inversions and IGW breaking in downslope windstorms, researchers have generally resorted to modeling studies focusing on either the importance of IGW breaking in continuously stratified systems or the applicability of RGSW theory in two-layer hydraulically controlled flow. While many numerical studies have successfully applied the IGW breaking model (Lilly and Zipser 1972; Clark and Peltier 1977; Peltier and Clark 1979; Doyle et al. 2000) or the RGSW model (Gohm et al. 2008; Flamant et al. 2002; Drobinski et al. 2001) to downslope windstorms, the groundwork for analogies between hydraulic theory (RGSW models) of downslope windstorms and continuously stratified systems began with the studies of Durran (1986) and Smith (1985). More recently, Vosper's (2004) modeling study included both IGW breaking simulations and hydraulic jump simulations. His results (see his Fig. 9) may be thought of as extension of Houghton and Kasahara's (1968, see their Fig. 3) for two-layer flows in which the upper layer is stratified and the lower layer is neutral. Jiang et al. (2007) also modeled the importance of an upstream inversion. The authors of this study indicate that the shallow water mode is dominant in their experiments; however it is not possible to ascertain to what extent IGW breaking above the lee slope (see the isotherms at the top of the plots in their Fig. 14) plays a role in their experiments.

Despite recent progress, many uncertainties remain regarding the distinction between downslope windstorms associated with elevated inversions and those associated with IGW breaking. Some observation studies suggest that diurnal heating may be important because changes in low-level inversion properties affect the formation and decay of windstorm events. For example, studies in the lee of the Sierra Nevadas (Zhong et al. 2008; Jiang and Doyle 2008) and in the lee of the Andes (Seluchi et al. 2003; Norte 1988) indicate an afternoon preference for increased downslope winds. In contrast, downslope windstorms over the front range of the Rocky Mountains are observed more frequently between 0000 and 0700 LST (Miller et al. 1974). Modeling studies addressing the effects of surface heat fluxes on downslope windstorms have primarily focused on nonhydrostatic trapped lee-wave rotors (Doyle and Durran 2002; Jiang et al. 2006; Smith et al. 2006) or the IGW breaking regime (Smith and Skyllingstad 2009; Ying and Baopu 1993). To date, no observational or modeling studies have focused on the influence of surface heat fluxes on downslope windstorms induced by either a subcritical to supercritical transition of the barotropic interfacial mode, or a mechanism intermediate to the IGW breaking and the RGSW mode.

Our main goal in this study is to examine how inversion height alters the characteristics of a downslope windstorm when background conditions favor internal wave breaking. We extend these cases by including scenarios with surface heating and cooling to determine how changes in the near surface stability affect cases with low-level inversions. Results are qualitatively compared with recent observations of downslope windstorms over the Falkland Islands (Mobbs et al. 2005).

The paper is structured as follows. A description of the large eddy simulation (LES) model is presented in section 2. Results are presented next in section 3 for

FIG. 1. Schematic showing the channel flow configuration used in the simulations.

TABLE 1. List of inversion height experiments used in section 3 and their inversion heights and inversion strengths.

	z_i (m)	$\Delta\theta$ (K)
No inversion	—	—
Low inversion	900	8
Medium inversion	1800	8
High inversion	3000	8

a comparison of cases with and without an inversion at various heights. Next the criteria for downslope windstorm formation in intermediate cases is compared to that of IGW breaking and the role of wave reflection is explored using rigid lid cases. The Falkland Islands dataset is analyzed in section 4 for evidence of modulation of downslope windstorm behavior with respect to inversions and diurnal time scales. In section 5 we apply surface heating and cooling to low inversion and medium inversion height cases along with experiments used to discern katabatic contributions to lee-flow behavior. Summary and conclusions are given in section 6.

2. Model introduction and setup

Experiments were performed using a modified version of the LES model described in Skyllingstad (2003) and used in Smith and Skyllingstad (2005) and Smith and Skyllingstad (2009). This model is based on the Deardorff (1980) equation set, with the subgrid-scale model described by Ducros et al. (1996). Pressure in the model is calculated using a compressible pressure solver (Klemp and Wilhelmson 1978). Terrain in the LES model is prescribed using a shaved cell approach described in Adcroft et al. (1997) and Steppeler et al. (2002).

Simulations were conducted using a narrow channel domain with periodic boundaries in the cross-slope and alongslope direction (Fig. 1). A sponge layer is used in the alongslope direction in the first 10 km of the domain to return the flow to an unperturbed upstream condition (Bacmeister and Pierrehumbert 1988). Further details of the numerical model and the surface friction condition are presented in Smith and Skyllingstad (2009). A two-dimensional ridge obstructing the flow was based on the Witch of Agnesi profile

$$h(y,z) = \frac{ha^2}{y^2 + a^2} \tag{5}$$

for a mountain of height $h = 600$ m, and half-width $a = 4000$ m. An idealized initial state is prescribed with constant static stability of $N = 0.01\ \mathrm{s}^{-1}$. The streamwise velocity v increases linearly from 5 to 11.5 m s^{-1} at 13 km. Aside from small random perturbations used to initialize turbulence, there is no initial spanwise velocity, and no spanwise or streamwise variation of velocity. Temperature inversions, if present, are centered at $z_i = 900$, $z_i = 1800$, and $z_i = 3000$ and have a thickness of 200 m. Using the velocity at crest level of 5 m s^{-1} and the free troposphere stability, $N = 0.01\ \mathrm{s}^{-1}$, a nondimensional mountain height of $Nh/v = 1.2$, and a nondimensional mountain width of $Na/v = 8$ were prescribed for our simulations. Mountain characteristics were selected to allow for qualitative comparisons of model results with observations from the Falkland Islands (Fig. 5). A relatively small terrain feature also allows for more direct interaction between boundary layer turbulence and terrain-induced flows.

Domain size was set to $80 \times 6480 \times 300$ grid points in the alongslope, cross-slope, and vertical directions, respectively, with grid resolution of 15 m in all directions below 3 km. Above 3 km, the vertical grid spacing stretches from 15 to 170 m at the model domain top. The total domain size was 1.2 km $\times$ 97.2 km $\times$ 13.1 km. A test simulation with a doubling of the channel width to 26.2 km did not produce results significantly different from the standard domain, suggesting that lateral eddy scales were adequately represented. The mountain was centered at $y = 58.3$ km, slightly past the centerpoint in the streamwise direction. In cases with a surface heat flux, heating was applied throughout the entire domain for the duration of the experiment domain unless otherwise indicated. (A summary of all experiments can be found in Tables 1 through 4.)

3. Numerical experiments on inversion height

We first examine the role of inversion height in determining the lee-flow response by conducting a set of four cases as described in Table 1, beginning with a case with no inversion and then three cases with progressively higher inversion height. Cross-section plots of streamwise velocity overlaid with contours of potential temperature showing the evolution of these four cases are shown in Fig. 2. In this figure we chose to present results at dynamically important times in the flow evolution. Like other investigators (Lamb 1994), we note that the experiments do not achieve steady state though

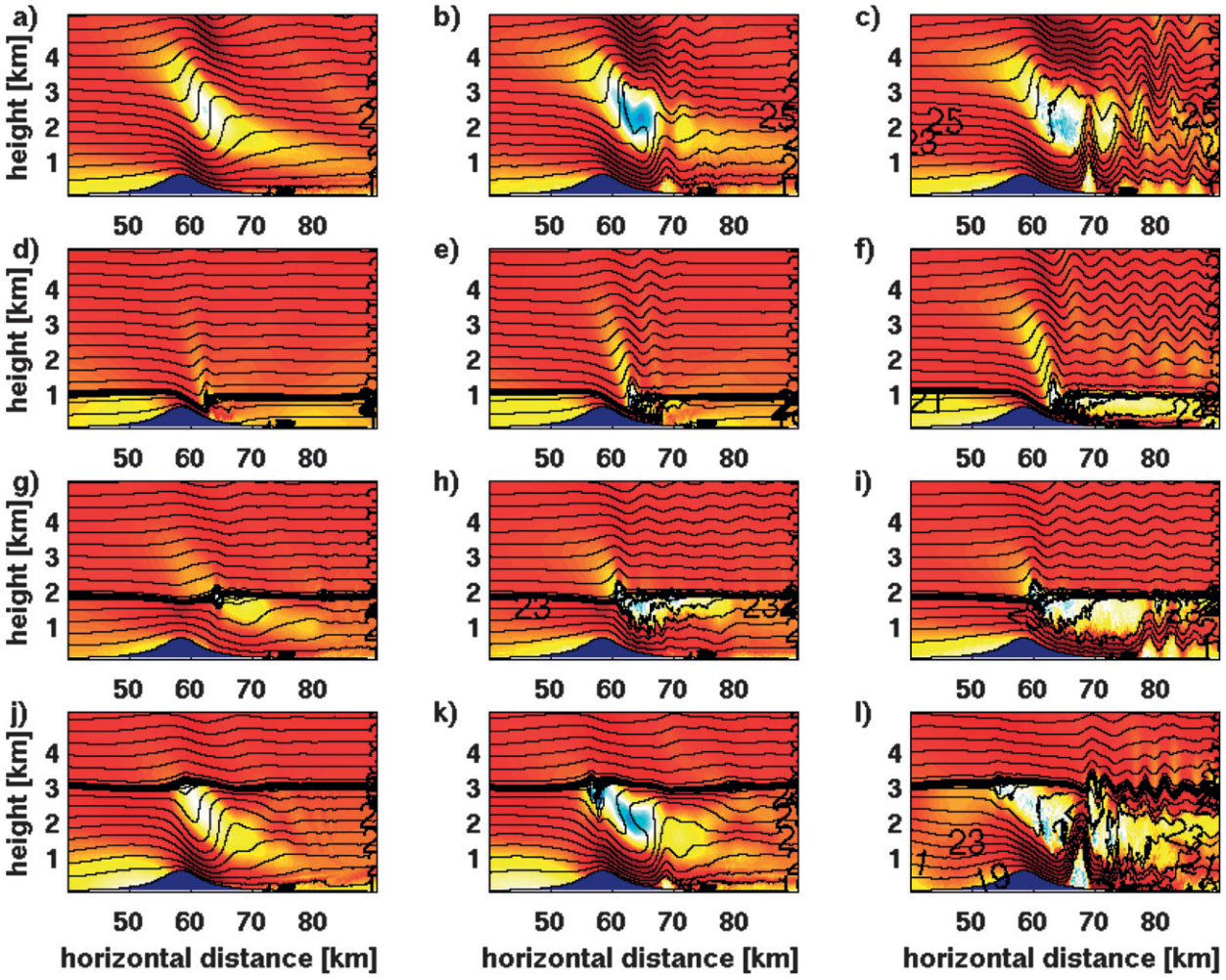

FIG. 2. Close-up view of streamwise velocity (shading in m s^{-1}) and potential temperature (lines of constant °C) for the no inversion case at (a) $t = 140$ min, (b) $t = 240$ min, (c) $t = 360$ min; low inversion case ($Nh/v = 1.2$, $z_i = 900$ m) at (d) $t = 20$ min, (e) $t = 40$ min, (f) $t = 180$ min; medium inversion case ($Nh/v = 1.2$, $z_i = 1800$ m) at (g) $t = 100$ min, (h) $t = 240$ min, (i) $t = 360$ min; and high inversion case ($Nh/v = 1.2$, $z_i = 3000$ m) at (j) $t = 80$ min, (k) $t = 120$ min, (l) $t = 200$ min. See following figure for colorbar.

we ran them until fully developed. We do not present all experiments at similar times because each case is governed by a different set of physics. For flow dominated by linear IGW, a suitable nondimensionalization might be $t \times v/a$, while for barotropic RGSW flow a suitable nondimensionalization might be $t \times c/a$, where the barotropic wave speed c is defined as the denominator of the Froude number [(3)]. For the cases presented herein that exhibit both IGW and RGSW physics, neither nondimensionalization would be strictly correct. The IGW case presented below (Fig. 2c) is shown at comparable similar nondimensional time ($t \times v/a = 27$) as in other experiments (e.g., Vosper 2004, his Fig. 2 presented at $t \times v/a = 24$). A further consideration regarding the evolution of flow in these experiments is that the boundary layer height is constantly evolving during the experiment and of the same order of magnitude as the ridge height. The perturbation recycling inflow condition has not previously been applied to mountain wave studies in which ridge height is comparable to boundary layer height. All variables presented in the plots are instantaneous at a single cross section in the model domain unless otherwise specified as being averaged. Averaging procedures are detailed in the appendix.

In the no inversion case, Figs. 2a–c show times when a self-induced critical level near $z = 2.5$ km becomes buoyantly unstable and generates a breaking wave with considerable turbulence. This experiment is broadly comparable to the basic case presented in an earlier study (Smith and Skyllingstad 2009) except with shear added to help avoid elevated secondary breaking

regions. Just before the onset of IGW breaking the isotherms become vertical and begin to overturn (Fig. 2b), generating increasing turbulence aloft between $z = 2$ and 3 km over the lee side of the ridge. Streamwise velocity in this region shows a typical nonlinear amplified gravity wave response with a large zone of trapped, stagnant air with near-zero mean streamwise velocity. Beneath this stagnant layer, winds increase along lee surface of the mountain, forming a jet that abruptly transitions to a train of rotors (Fig. 2c). The trapped lee-wave rotors (we define a rotor as a negative streamwise surface velocity) are partly due to the nonhydrostatic forcing of the mountain on the flow ($Na/U = 8$) and partly due to nonlinear interactions with the IGW breaking and stagnation zone. While not the topic of this paper, we note that the launching of dispersive waves by the stagnation zones is similar to results presented in Jiang et al. (2007, their Fig. 14b). Broad mountains generally tend to force hydrostatic waves but, because of interactions with the self-induced stagnation zone in highly nonlinear cases, can also force dispersive waves. Turbulence from the stagnation zone is not strong enough to mix out negative streamwise velocities in the rotor nearest to the mountain.

In the low inversion case, Figs. 2d–f shows the time period when the barotropic mode on the inversion at $z_i = 900$ m transitions from subcritical to supercritical. Breaking is evident on the upstream side of the incipient hydraulic jump and the fully developed flow descends well past the base of the slope and is almost entirely beneath a stagnation zone, which is in turn constrained below the inversion at $z_i = 900$ m. Downstream, the inversion then returns relatively intact to $z_i = 900$ m. Both hydrostatic, vertically propagating IGWs and trapped lee waves are evident above the inversion but play only a small role in the slope flow.

The medium inversion height case (Figs. 2g–i) also shows both a weak hydrostatic IGW and lee-wave response above the inversion, similar to the low inversion case. An instability on the inversion (Fig. 2g) is associated with the generation of a self-induced critical layer (Fig. 2h) and the resultant leeside downslope flow is much deeper than the low inversion case and the inversion does not extend down the slope. The leeside jet in this case is formed by compressing the stratified layer below the inversion, rather than by forcing the inversion down the slope as in the low inversion case. Rotors are produced in line with the no inversion case, but they are located much further downstream and their height is constrained to be less than the inversion. The mechanism for the generation of the lee slope flow is neither strictly IGW breaking nor RGSW transition. While wave reflection seems to be the dominant mechanism, the creation of a horizontal velocity defect and splitting of the inversion by pressure gradient and nonlinear advection associated with the flow response to the topographical perturbation is also important. In the pocket of neutrally stratified stagnant air, which has an inversion and strong horizontal velocity gradients both above and below, instabilities may spontaneously occur and grow. Once turbulence is initiated, the stagnation region grows because of shear production of TKE along the bottom of the stagnation zone and top of the lee jet. The entire upstream flow from the surface up to the inversion is constrained between the mountain and the stagnation zone, resulting in high surface velocities on the lee slope.

Increasing the height of the inversion to 3 km (Figs. 2j–l) produces a large rotor and self-induced stagnation zone similar to the results from the no inversion case. The dominant physics for both the high inversion case and the no inversion case (Fig. 2c) appears to be IGW breaking, though more turbulence is present in the lee of the high inversion case, along with reduced IGW activity aloft. The nondimensional mountain height, $Nh/U = 1.2$, corresponds to a hydrostatic vertical wavelength,

$$\lambda_z = 2\pi\frac{U}{N} = 3142\,\text{m}, \tag{6}$$

and a corresponding level of IGW breaking of $\frac{3}{4}\lambda_z = 2356$ m, which is below the height of the inversion, at $z_i = 3000$ m. These results suggest that the IGW breaking dynamics are relatively unaffected by the presence of the inversion, and the lee flow response for the no inversion and high inversion cases are relatively similar. More generally, the ratio of hydrostatic vertical wavelength (or level of IGW breaking), to inversion height, λ_z/z_i, is very useful in describing the flow for nonlinear IGW cases (i.e., $Nh/U > 1$).

Results shown in Fig. 2 indicate that the low and high inversion cases can be explained by transcritical flow and breaking IGW mechanisms, respectively. The low inversion case is the only one that behaves like a barotropic shallow water system with a subcritical to supercritical transition near the ridge crest. In all of the cases the upstream Froude number based on (3) is less than 1. However, in the low inversion case, z_i decreases below 100 m as the flow moves over the mountain ridge forcing the local Froude number to increase above 1 and the flow to transition to a supercritical state. Inversion heights in the medium and high inversion cases are too high for this transition. For the high inversion case, IGW breaking produces a strong wave reflection with leeside flow similar to the case without an inversion.

The medium inversion height case presented in Fig. 2i seems to contain characteristics of IGW breaking and the shallow water mode hydraulic mode. Since the

TABLE 2. List of mountain height experiments and their mountain height and nondimensional mountain height.

h_{mtn} (m)	Nh/U	Inversion present	Downslope windstorm
200	0.4	Y	N
250	0.5	Y	N
350	0.7	Y	Y
450	0.9	Y	Y
600	1.2	Y	Y
200	0.4	N	N
250	0.5	N	N
350	0.7	N	N
450	0.9	N	N
600	1.2	N	Y

criteria for downslope windstorms occurrence in shallow water flows is fairly well known, as is the criteria for continuously stratified cases, an interesting question to ask is whether either of these two criteria apply to the medium inversion height case. A series of numerical experiments were run with a reduced mountain height and nonlinearity parameter, Nh/U, to better elucidate the role of IGW breaking in the medium inversion case. These cases, which are listed in Table 2, were conducted both with and without an inversion whose inversion strength, $\Delta\theta = 8$ K, and inversion height, $z_i = 1800$ m, were the same as the medium inversion case presented above. These experiments in this section were run at 25-m resolution with the same domain size as those above. No significant differences between similar simulations run at 25-m resolution and those run at 15-m resolution were noted.

Results from cases with $h_{mtn} = 200$ m ($Nh/U = 0.4$) and $h_{mtn} = 450$ m ($Nh/U = 0.9$) with and without an inversion are presented in Fig. 3. As expected, in the cases without an inversion, only large mountains (Fig. 2c) produce downslope windstorms, and in all cases with $Nh/U < 1$ (Figs. 3a,b) IGWs do not overturn and create a self-induced stagnation zone. This result is consistent with the notion of Nh/U as a measure of the nonlinearity of the response (Clark and Peltier 1977) and also indicates that Scorer parameter layering (Klemp and Lilly 1975) is not important in our simulations. However, the mountain height threshold for breaking with an inversion present is significantly lower than it is for cases lacking an inversion. In fact, inversion cases with $Nh/U = 0.7$ and $Nh/U = 0.9$ (Fig. 3d) resulted in a downslope windstorm with significant lee extent. For the inversion case with $h_{mtn} = 200$ m and $Nh/U = 0.4$ (Fig. 3c) a perturbation develops on the inversion but never leads to a self-induced critical layer or a jet. The inversion cases with $Nh/U = 0.7$ and 0.9 (Fig. 3d), similar to the $Nh/U = 1.2$ case presented above (Fig. 2c), also do not exhibit a subcritical to supercritical transition of the shallow water mode and thus bear further examination since the nonlinearity parameter, Nh/U, is less than unity as well indicating that the IGW should not overturn and create a self-induced stagnation zone (Lin and Wang 1996).

In the medium inversion case (Fig. 2i), the flow below the inversion behaves much like a shallow water hydraulic transitional flow, even though the fluid is stratified. Vertical waves in this case appear to be trapped below the inversion, suggesting a reflective layer somewhat like examples given in Durran (1986) for abrupt changes in the Scorer parameter N/U. Smith (1985) examined flows that have a similar hydraulic behavior and developed a set of criteria for flow transitions based on the scaled height of the obstacle, Nh/U, and the level of a dividing streamline or reflection, NH/U, where H is the height of the streamline. For cases where the dividing streamline is a rigid lid, flow behavior can also be determined using a mode number,

$$K = \frac{DN}{\pi U}, \tag{7}$$

where D is the height of the rigid lid. Lamb (1994) and Skyllingstad and Wijesekera (2004) show that for sufficiently high Nh/U, values of K near integer values of 1 and 2 will generate strong leeside flows, whereas intermediate K values (e.g., 1.5) lead to a weak leeside response. Similarly, a K value of 1 is roughly consistent with results from Smith (1985; assuming D is the dividing streamline height) who determined that this value would lead to a transitional flow if $Nh/U > 0.5$. If we assume that the medium inversion acts as a rigid lid reflector, then $K = 1.15$, which is near a value of 1 and should generate a strong lead side response for $h > \sim 250$ m based on the theory presented in Smith (1985).

To test this idea further, a series of experiments were conducted replacing the inversion in the simulations with a rigid lid boundary condition (Table 3). Four cases were examined as shown in Fig. 4, for a rigid lid at 1800 and 2500 m. The 2500-m case was selected to represent the effects of a self-induced critical layer and wave breaking as produced in the stratified reference case (Fig. 2c). Cases are examined for a 200- and 450-m ridge, following the inversion case presented in Fig. 3. When the rigid lid is placed at 1800 m, a transitional flow is produced with $h = 450$ m (Fig. 4d) suggesting, qualitatively, that the key effect of the inversion is to act as a reflective cap. Reduction of the mountain height to 200 m (Fig. 4c) produces a weaker response consistent with the 1800-m inversion case, although here the flow has more strength. The comparatively weaker leeside flow in the inversion case (Fig. 3c) could be explained by the motion of the

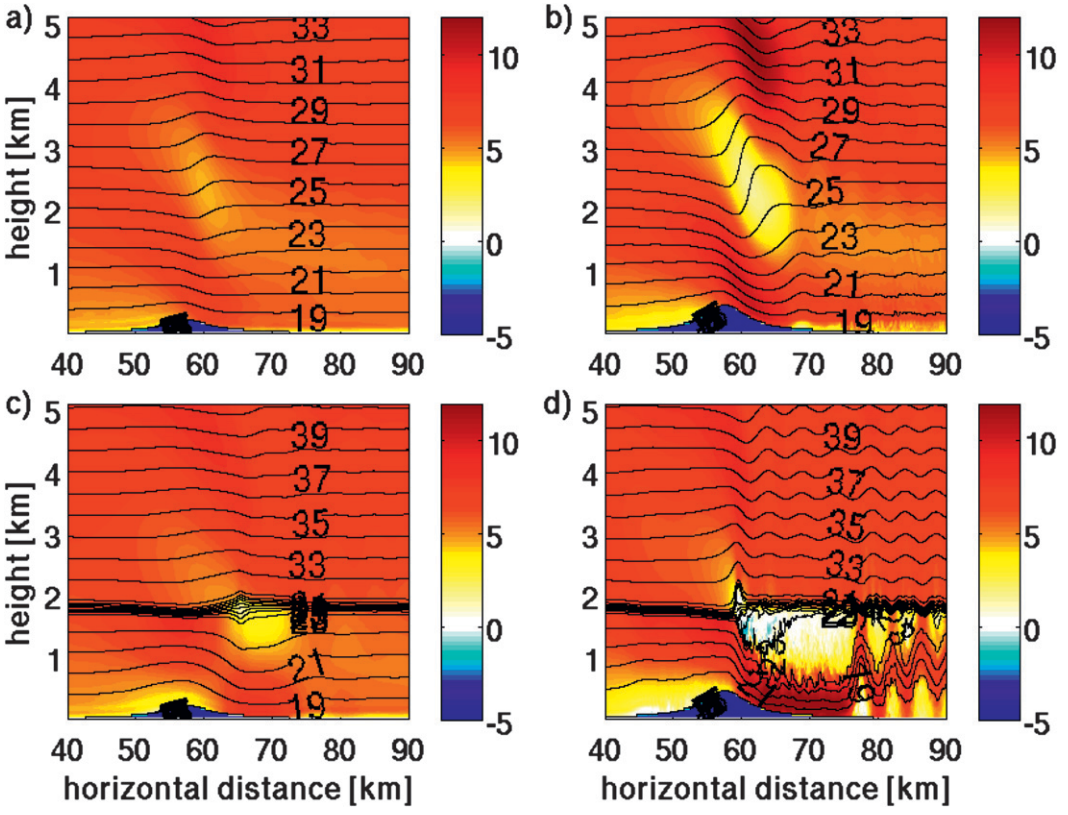

FIG. 3. Close-up view of streamwise velocity (shading in m s^{-1}) and potential temperature (lines of constant °C) for the (a) no inversion $Nh/v = 0.4$ case at $t = 360$ min, (b) no inversion $Nh/v = 0.9$ case at $t = 360$ min, (c) inversion $Nh/v = 0.4$, $z_i = 1800$ m case at $t = 300$ min, and (d) inversion $Nh/v = 0.9$, $z_i = 1800$ m case at $t = 480$ min.

inversion and vertical removal of energy by internal waves, which is not possible in the rigid lid case.

Increasing the inversion height to 2500 m generates a similar outcome, but with a very strong transitional flow response for $h = 450$ m (Fig. 4b) indicating that the effects of wave breaking may be compounding the reflection of wave energy from the rigid lid. Comparison of this result with the continuously stratified case shown in Fig. 3b demonstrates how vertical propagation of wave energy above the 2500-m level in the continuous case limits the surface leeside response. Flow over the $h = 200$ m terrain in the 2500-m rigid lid case (Fig. 4a) produces a strikingly weaker flow, with vertical displacements limited to a few hundred meters and almost no leeside acceleration. This result is in basic agreement with Smith (1985), which indicates that a higher terrain feature is needed for a strong hydraulic response given the 2500-m level of reflection.

4. Observations of downslope windstorms on the Falkland Islands

Given the disparate causes of downslope windstorms and the various resultant lee flow regimes, it is useful to examine observations of flow over a low 2D ridge for assurance that the model is reasonably close to actual flows. In addition, we wish to see if lee jet length varies according to inversion height and surface heat fluxes. The dataset of Mobbs et al. (2005) taken on the Falkland Islands was chosen for this analysis because of the intense turbulent episodes that occur at the Mount Pleasant Airfield, a few kilometers west-southwest (WSW) of station 5 (Fig. 5). From the dataset we selected three stations, which, for northerly flow were located upstream (station 24), near downstream (station 5), and far downstream (station 1) of the ridge. Surface wind velocity was collected at these stations from November 2000 to October 2001 and averaged over 10-min periods.

TABLE 3. List of rigid lid experiments including the height of the rigid lid and the mountain height.

h_{mtn} (m)	Height of rigid lid (m)
200	1800
200	2500
450	1800
450	2500

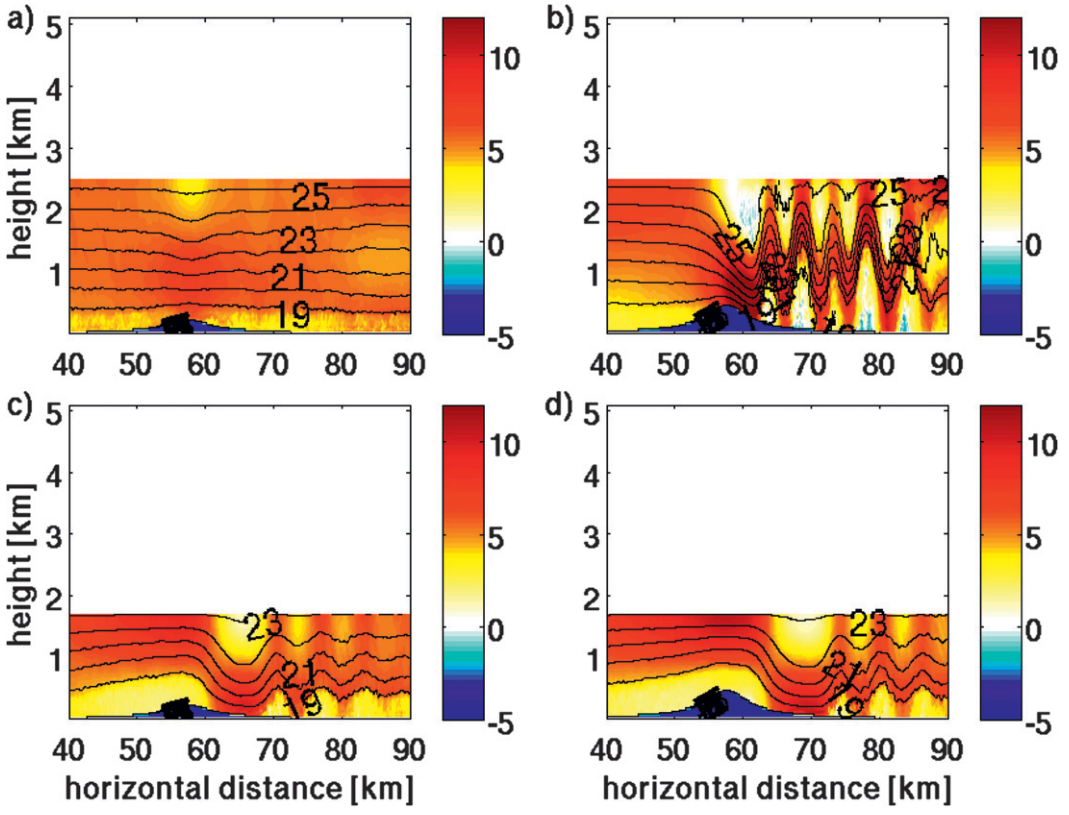

FIG. 4. Close-up view of the rigid lid cases (shading in m s^{-1}) and potential temperature (lines of constant °C) for the case with (a) rigid lid at 2500 m and h_{mtn} = 200 m at t = 360 min, (b) rigid lid at 2500 m and h_{mtn} = 450 m at t = 280 min, (c) rigid lid at 1800 m, and h_{mtn} = 200 m at t = 360 min, and (d) rigid lid at 1800 m and h_{mtn} = 450 m at t = 360 min.

The diurnal variation of northerly and southerly wind events, defined as $v > 10$ m s^{-1} for the stations downstream of the ridge and $v > 5$ m s^{-1} for the station upstream of the ridge, is shown in Fig. 6. The percentage of total number of events by 10-min bins is calculated by summing all wind events by bin and normalizing by the total number of events in each wind direction. The total number of northerly events for stations 5 and 24 and southerly events for station 5 binned by 10-min intervals was 1809, 6301, and 3915, respectively. All stations on both sides of the ridge show a propensity for southerly and northerly wind events to occur in early afternoon, most likely due to downward mixing of momentum from aloft as the boundary layer height increases from surface heating. A preferential speedup of the flow over the ridge at nighttime is indicated by the secondary maximum of northerly events at the downstream station, 5, with no associated increase in northerly wind events for the upstream station, 24. The presence of Mt. Simon to the north of the main Wickham range on the East Falkland Island make a similar analysis of southerly wind events problematic.

Of all northerly wind events, 74% occur only at the near downstream station 5, and only 26% extend as far downstream as station 1 as well (Fig. 7a, which contains 2469 total events binned by 10-min intervals). The

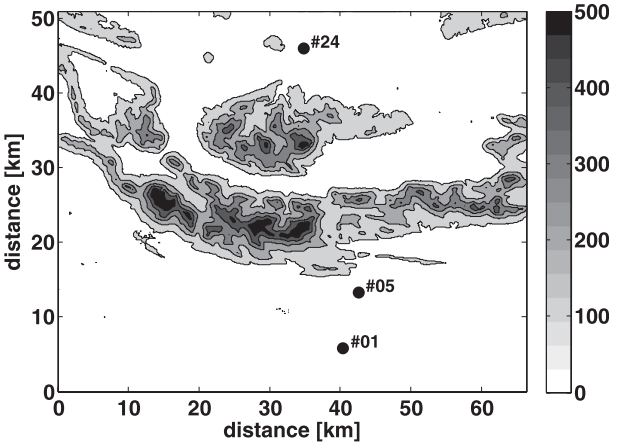

FIG. 5. The location of the stations on the East Falkland Island used in this analysis. Terrain height (m) is shaded.

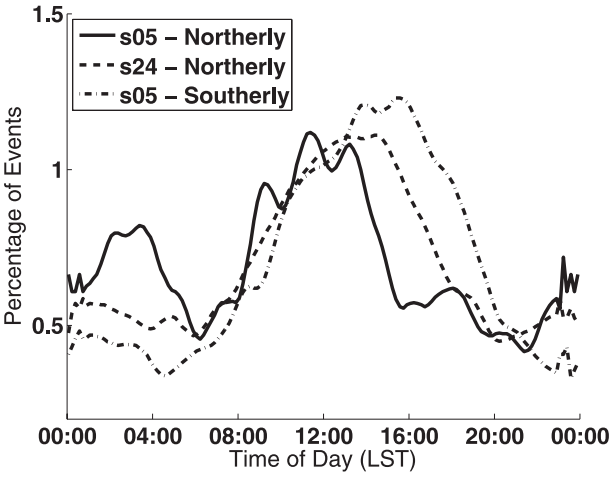

FIG. 6. Diurnal variation of northerly and southerly wind events at station 5 and northerly wind events for station 24.

synoptic soundings, taken downstream of the ridge, were used to determine the extent to which inversion strength affected the presence of downslope windstorms and controlled jet length. The inversion strength $\Delta\theta$ was found by searching the sounding for any increase in temperature with height, between 0.2 and 5.0 km above ground, with a depth greater than 20 m and a strength greater 0.1 K. Inversions separated by layers of less than 100-m depth were combined and only the strongest inversion was kept in soundings that contained multiple well-separated inversions. We looked at only those soundings that were taken at the synoptic times when the dynamical forcing was consistent with possible formation of a downslope windstorm event; that is, the velocity at ridge-top level v_{rt} was greater than 5 m s^{-1}. Each surface wind velocity measurement was correlated with the inversion strength of the nearest sounding, if any was present within 2 h of the surface measurement taken to produce the plots in Figs. 7b,c. Soundings with weak inversions tend to result in a jet with limited downstream extent (Fig. 7b, which contains 251 total events binned by 10-min intervals), while soundings with strong inversions are relatively more likely to result in windstorms with significant downstream extent (Fig. 7c, which contains 137 total events binned by 10-min intervals). Two reservations about this correlation should be noted: the soundings were actually taken downstream of the ridge so the ridge-top-level velocity and low level inversion strength may not be representative of their upstream values, and it may not be appropriate to use a correlation window of 2 h since synoptic conditions are constantly changing.

Two specific downslope windstorm events are useful in illustrating the type of behavior described above.

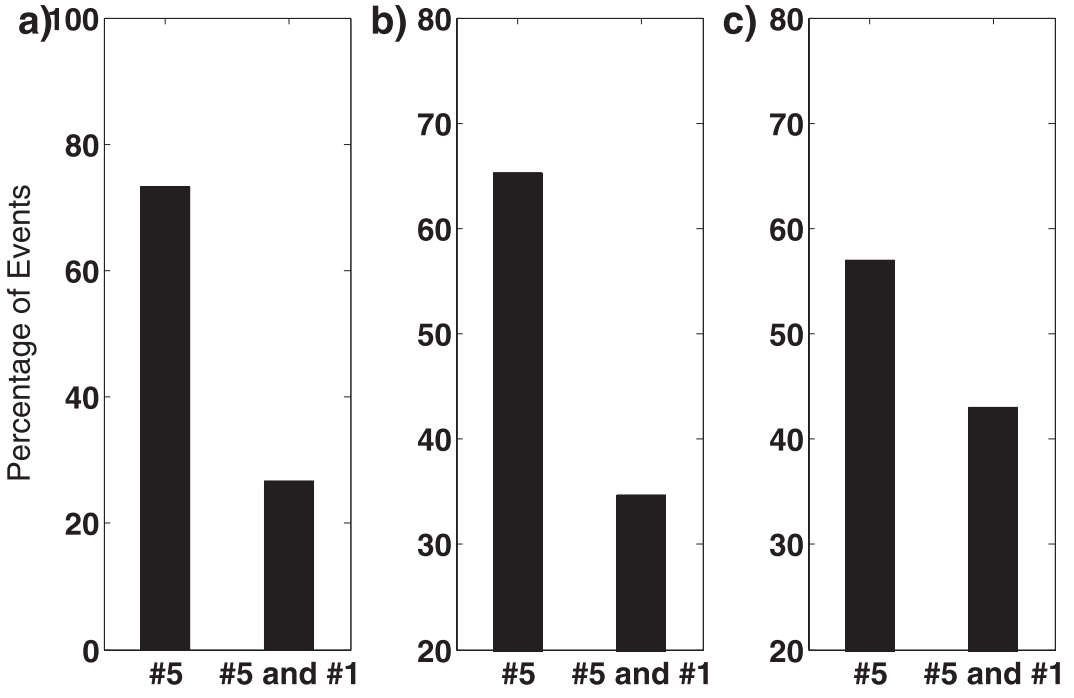

FIG. 7. Percentage of (a) all northerly wind events which occur at station 5 only, and stations 5 and 1 contemporaneously, and percentage of northerly wind events whose correlated soundings have (b) $\Delta\theta < 4$ K and (c) $\Delta\theta > 4$ K which occur at station 5 only and stations 5 and 1 contemporaneously.

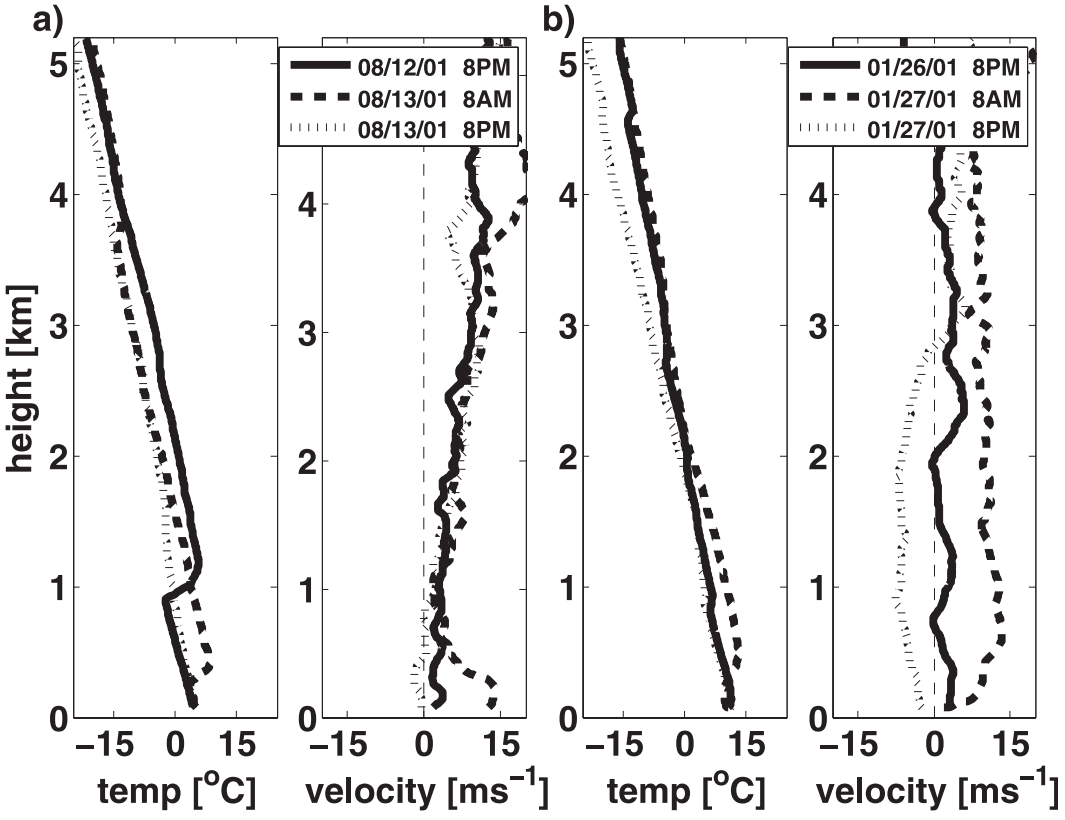

FIG. 8. (left) Temperature and (right) northerly wind velocity vs height for the soundings taken between (a) 2000 LST 12 Aug to 2000 LST 13 Aug 2001 and (b) 2000 LST 26 Jan to 2000 LST 27 Jan 2011.

Wind velocity aloft changed little during the event of 13 August 2001, while a strong inversion was present near 1 km (Fig. 8a) before and possibly during this event. Strong northerly winds at only the near-ridge downstream station 5 began just after 0000 LST and lasted until around 0800 LST, while little change in the upstream surface station 1 occurred during this time (Fig. 9a). The event that occurred on the mornings of 27 January 2001 (Fig. 9b) was characterized by a much longer jet, in which both downstream stations, 1 and 5, reported high wind velocities throughout the night while the upstream station 24 saw only a slight increase of wind speed during this time. Conditions aloft during this time (Fig. 8b) were marked by large increase in wind velocity and an increase in inversion strength near ridge-top level. Since many downslope windstorm events occurred contemporaneously with a changing of inversion strength or height it is difficult to attribute the onset or decay of any event to nighttime surface cooling alone, but observations from these two events are consistent with the following two points: downslope windstorms may begin and subside with little change in ridge-top-level velocity evident from the soundings, and an increase in low level inversion strength and increase in ridge-top-level velocity can lead to an increase of jet length, especially during nighttime.

5. Numerical experiments on surface heating

Observations of downslope windstorms are not entirely clear, so we turn to numerical experiments of flow over a simplified low 2D ridge to further explore the effect of surface heat fluxes on downslope windstorms. Previous studies of the influence of surface heat fluxes on IGW breaking cases (Smith and Skyllingstad 2009) and the above study on how the mechanism of downslope windstorm formation varies according to inversion height suggests that diurnal variation of downslope windstorm behavior may depend greatly on the presence of inversions. Inversion strengths and heights presented here (Table 4) are consistent with the observations taken on the Falkland Islands (Mobbs et al. 2005) and analyzed above.

We first present streamwise velocity for the low inversion case, similar to the hydraulically controlled case presented before (Fig. 2f), with 200 W m^{-2} surface

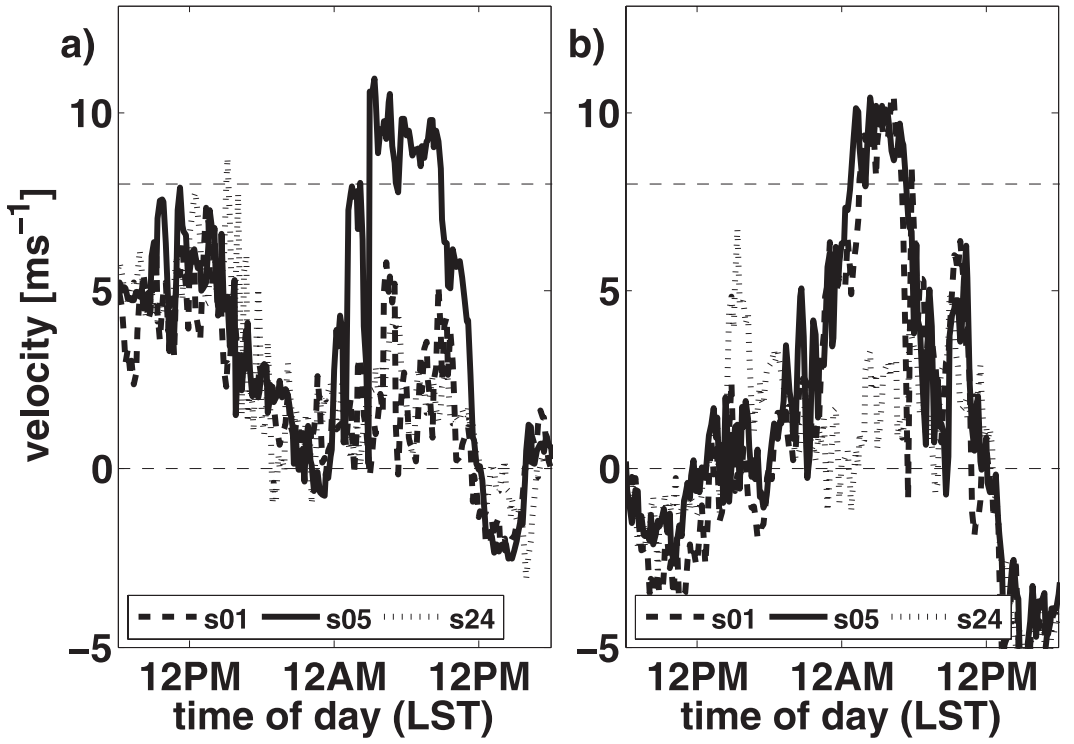

FIG. 9. Northerly wind velocity at stations 1, 5, and 24 vs time for (a) 0600 LST 12 Aug to 1800 LST 13 Aug 2001, and (b) 0600 LST 26 Jan to 1800 LST 27 Aug 2001.

heating applied throughout the simulation (Fig. 10a). The addition of surface heating has resulted in a shortened surface jet and more turbulent surface layer. The application of surface cooling (Figs. 10b–d) after 4 h of heating of 200 W m^{-2}, results in a transition that occurs relatively quickly. After 20 min of surface cooling (Fig. 10b), the surface jet has already begun to restratify in the lee of the ridge and has extended 10 km farther downstream relative to the heating case from which this case was initialized. After 2.5 h of surface cooling (Fig. 10d), the inversion downstream of the jump is relatively weak compared to its undisturbed upstream strength, and a significant portion of it remains in the strongly stably stratified surface jet. Flow blocking and a drainage flow have created a pocket of negative surface velocities on the upstream side of the ridge, while in the far downstream solitary like waves are present and slowly propagate back toward the ridge.

The application of surface heating of 200 W m^{-2} to the medium inversion height case results in a lee-flow response very different from the no heating case presented previously (Fig. 2i). The complete lack of a downslope jet (Fig. 11a) is due to reduced stratification in the boundary layer, which has prevented a wave response over the ridge. Lower values of N below the inversion reduced both Nh/v and NH/v, preventing the formation of a transitional flow (Smith 1985; Lamb 1994). For the surface cooling case (Figs. 11b–d), which was run using 6 h of 200 W m^{-2} of surface heating followed by 200 W m^{-2} of surface cooling for 6 h, the transition from a turbulent boundary layer to a downslope jet begins with a restratification of the boundary layer beneath the inversion (Fig. 11b), resulting in a gradual strengthening of the transitional flow as NH/v increases. The overturning isotherms begin to generate turbulence in the stagnation zone, which begins to grow downward and downstream because of large vertical gradients in horizontal velocity, forcing the lee flow below and forming a surface jet (Fig. 11d). The fully developed jet extends far downstream, is strongly stratified in the surface layer, and lacks the

TABLE 4. List of experiments presented in section 5 and their inversion heights, inversion strengths, and applied surface heat fluxes.

	z_i (m)	$\Delta\theta$ (K)	Surface heat flux (W m^{-2})
Low inversion heating	900	8	+200
Low inversion cooling	900	8	−200
Medium inversion heating	1800	8	+200
Medium inversion cooling	1800	8	−200

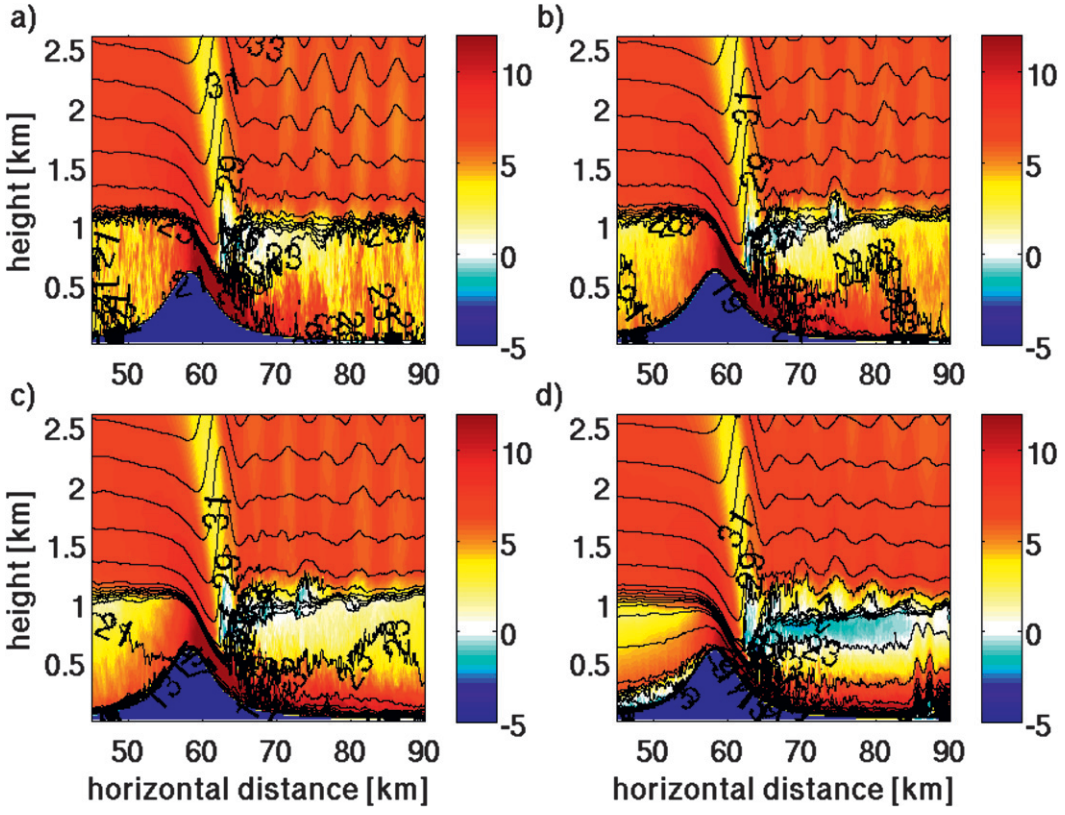

FIG. 10. Close-up view of streamwise velocity (shading in m s^{-1}) and potential temperature (lines of constant °C) for the (a) low inversion heating case ($Nh/U = 1.2$, $z_i = 900$ m) at $t = 180$ min and low inversion cooling case at (b) $t = 260$ min, (c) $t = 280$ min, and (d) $t = 390$ min.

downstream rotors that are present in the no heating case (Fig. 2i).

Additional simulations with surface heating constrained to either the upstream or downstream side of the ridge only reveal the role of stratification in the boundary layer acting to communicate the topographical perturbation to the inversion layer. The upstream heating case, similar to the case where heating is applied everywhere, results in no downslope jet at all, while the downstream heating case has only a small effect on the jet.

Further simulations with no mean flow velocity and surface cooling were used to explore the katabatic flow contributions to the lee jets for the surface cooling experiments. Drainage flows of approximately 200-m depth developed far downslope, with flow velocities of approximately 3 and 5 m s^{-1} for 50 and 200 W m^{-2} of surface cooling, respectively. In the low inversion case, the jet far downstream only showed a significant increase in flow velocity in the cooling case relative to the no heating case because of the contribution of the drainage flow. In the medium inversion case little contribution from the katabatic flows was evident anywhere in the lee jet.

6. Conclusions

The focus of this study was to examine how inversions impact the formation of downslope wind storms. Three downslope windstorm mechanisms were examined focusing on the height of the inversion and the development of self-induced critical layers and internal wave breaking. The first mechanism studied resembled two fluid barotropic hydraulic flows where the inversion is displaced vertically when moving over terrain. A second scenario examined depended on the inversion acting as a reflective barrier, leading to strong internal wave trapping. The last mechanism we simulated focused on the interaction between an inversion and internal wave breaking from a self-induced critical layer. Results from these simulations were used to interpret observations for evidence of modulation of jet length and occurrence with respect to surface heat fluxes and the presence of inversions.

Our initial set of experiments focused on four cases: low inversion, medium inversion, high inversion, and no inversion. The no inversion case, similar to the high

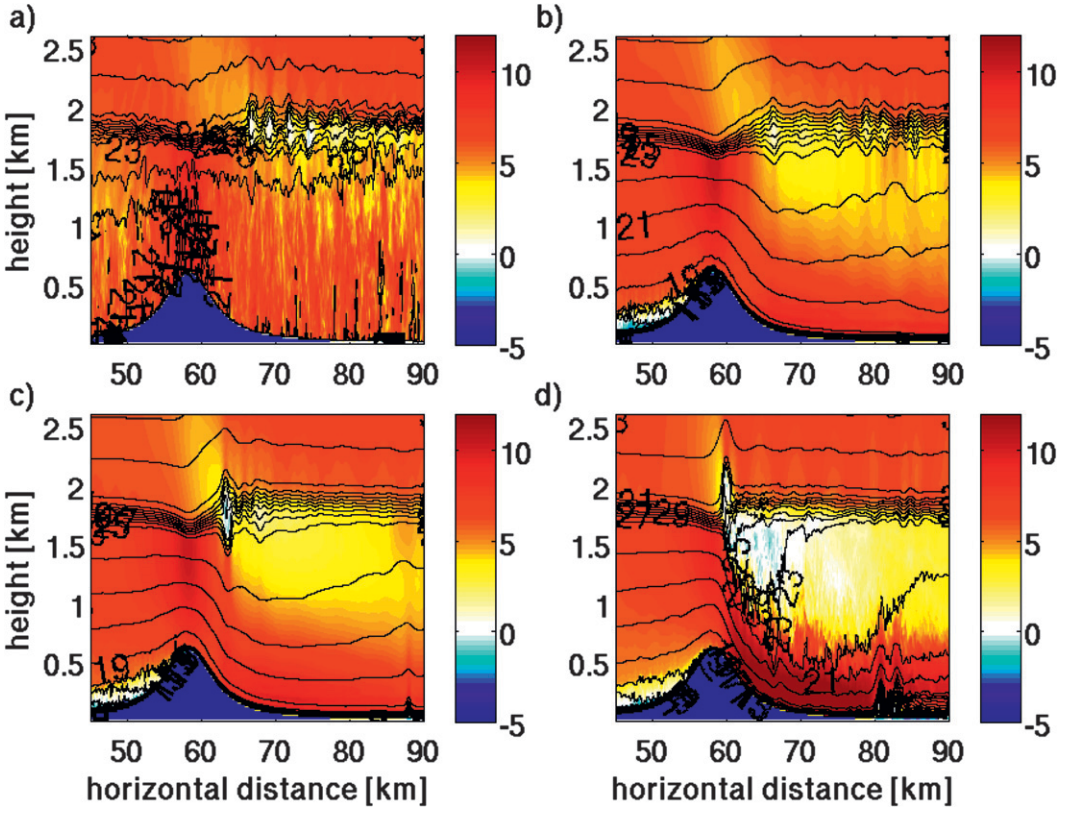

FIG. 11. Close-up view of streamwise velocity (shading in m s^{-1}) and potential temperature (lines of constant °C) for the (a) medium inversion heating case ($Nh/U = 1.2$, $z_i = 1800$ m) at $t = 300$ min and medium inversion cooling case ($Nh/U = 1.2$, $z_i = 1800$ m) at (b) $t = 420$ min, (c) $t = 520$ min, and (d) $t = 720$ min.

inversion case, resulted in IGW breaking, the creation of a stagnation zone and lee-slope jet of limited downstream extent. A hydraulic control point and transition of the shallow water mode over the ridge in the low inversion case resulted in a lee-slope jet and stagnation zone extending far down the slope with an absence of trapped lee waves. The medium inversion case resulted in the creation of a stagnation zone and downslope jet very similar to the hydraulic control case, but with little displacement of the inversion and most of the downslope flow coming from the stratified layer below the inversion.

We then presented a series of reduced mountain height experiments, with an inversion at the medium height and without an inversion, designed to test the theory of Smith (1985) and simulations presented in Lamb (1994) and Skyllingstad and Wijesekera (2004). As expected, IGW breaking occurred in the cases without an inversion only for $Nh/U > 1$. For cases with an inversion at the medium height, downslope windstorms occurred down to $Nh/U = 0.7$, indicating that nonlinear IGW breaking was not the sole dynamical reason for the lee-slope jet. Experiments conducted with a rigid lid suggest that the inversion in these cases acts as a reflective surface much like a critical level. Formation of increased leeside winds were found to depend on the inversion height and mountain height scaled by N/U, qualitatively agreeing with Smith (1985) and Lamb (1994).

Observations taken from the Falkland Islands were presented showing that downslope windstorm occurrence and lee-slope jet length varied on diurnal time scales and according to the presence of an inversion. Aside from a modulation of boundary layer height in the afternoon, which led to increased momentum transfer from aloft, downslope windstorm events preferentially occurred during nighttime (an interesting aside which was not explored herein is the presumed seasonal variation of SST and boundary layer stability due to variation of the ocean currents around the Falkland Islands). Events with significant downstream extent, which were relatively infrequent, tended to occur in conjunction with strong inversions, while events that occurred in conjunction with weak inversions were much more common and generally of limited downstream extent. A few specific events were presented that were indicative of the general trend: diurnal variations in downslope

windstorms do occur, sometimes with or without synoptic changes, and strong inversions tend to lead to lee-surface jets with significant downstream extent more often than weak inversions.

A second series of numerical experiments, in the context of the basic simulations and using observations from the Falkland Islands, explored the effect of surface heat fluxes on downslope windstorms that occurred in conjunction with a strong ridge-top-level inversion. In the low inversion case, surface heating was shown to reduce lee-jet length, while surface cooling resulted in an increase in jet length. The katabatic contribution to this jet length was fairly significant far away from the slope, which seems to be in agreement with observations from the Falkland Islands. In the medium inversion case surface heating led to a complete absence of downslope windstorms, consistent with a reduction in the N/U below the inversion. The application of surface cooling forced a transition to a downslope windstorm whose katabatic contribution was minimal.

Overall this study points to a lack of temporally appropriate upper air data to discern diurnal variations in downslope windstorm behavior from those variations that occur on synoptic time scales. A well-placed profiler would probably be quite useful to address this issue. It should be emphasized the simulations presented herein are limited in scope and it is not clear the extent to which the following conclusions might be generally applicable, particularly since all ridges exhibit spanwise heterogeneity, which has not been studied here. A number of points are raised by this research that may be of interest to those tasked to predict downslope windstorms in an operational environment.

1) Accurate estimates of upstream inversion height and the stratification below inversions are crucial for predicting downslope wind events.
2) Absent synoptic-scale changes in forcing, downslope windstorms over a low ridge may preferentially occur in the evening, especially for locations far downstream.
3) The downstream extent of an event, and its katabatic contribution, varies according to inversion strength and surface heating.

Acknowledgments. We are pleased to acknowledge the super-computer time provided by the National Center by Atmospheric Research, which is funded by the National Science Foundation. This research was funded by the National Science Foundation under Grants ATM-0527790 and OCE-751930. We thank Peter Sheridan at the Met Office for sharing the Falkland Islands data. We also wish to thank the anonymous reviewers for their help in strengthening the manuscript.

APPENDIX

Averaging Procedures

For the purposes of this study we define the average of a variable ϕ as follows:

$$\overline{\phi}(y,z) = \frac{1}{i_{\max} n_{\max}} \sum_{n=1}^{n_{\max}} \sum_{i=1}^{i_{\max}} \phi(x,y,z), \qquad \text{(A1)}$$

where the overbar denotes average. In this equation $i_{\max}$ is the number of points in the spanwise direction and $n_{\max}$ is the number of time steps over the 5-min averaging time. Turbulent kinetic energy (TKE) is calculated by using the spanwise mean

$$\phi_{\text{spanwisemean}}(y,z) = \frac{1}{i_{\max}} \sum_{i=1}^{i_{\max}} \phi(x,y,z) \qquad \text{(A2)}$$

to calculate perturbations about the spanwise mean

$$\phi'(x,y,z) = \phi(x,y,z) - \phi_{\text{spanwisemean}}(y,z) \qquad \text{(A3)}$$

and the average resolved eddy TKE is defined as

$$e' = \frac{1}{2}(u'^2 + v'^2 + w'^2), \qquad \text{(A4)}$$

and perturbation velocities are calculated as in (A3) and (A2), and the averaging is done in the spanwise direction as well as temporally as in (A1). Computing averages in this way removes the large-scale internal waves generated by the mountains, however smaller scale waves are still treated as ''turbulence.'' Nevertheless, this method yields turbulence fields that are consistent with buoyant and shear production of turbulence.

REFERENCES

Adcroft, A., C. Hill, and J. Marshall, 1997: Representation of topography by shaved cells in a height coordinate ocean model. *Mon. Wea. Rev.,* **125,** 2293–2315.

Bacmeister, J. T., and R. T. Pierrehumbert, 1988: On high drag states of nonlinear stratified flow over an obstacle. *J. Atmos. Sci.,* **45,** 63–80.

Belusic, D., M. Zagar, and B. Grisogono, 2007: Numerical simulation of pulsations in the bora wind. *Quart. J. Roy. Meteor. Soc.,* **133,** 1371–1388.

Clark, T. L., and W. R. Peltier, 1977: On the evolution and stability of finite-amplitude mountain waves. *J. Atmos. Sci.,* **34,** 1715–1730.

Deardorff, J. W., 1980: Stratocumulus-capped mixed layers derived from a three-dimensional model. *Bound.-Layer Meteor.,* **18,** 495–527.

Doyle, J. D., and D. R. Durran, 2002: The dynamics of mountain-wave-induced rotors. *J. Atmos. Sci.,* **59,** 186–201.

——, and Coauthors, 2000: An intercomparison of model-predicted wave breaking for the 11 January 1972 Boulder windstorm. *Mon. Wea. Rev.,* **128,** 901–914.

Drobinski, P., C. Flamant, J. Dusek, P. Flamant, and J. Pelon, 2001: Observational evidence and modeling of an internal hydraulic jump at the atmospheric boundary-layer top during a tramontane event. *Bound.-Layer Meteor.,* **98,** 497–515.

Ducros, F., P. Comte, and M. Lesieur, 1996: Large-eddy simulation of transition to turbulence in a boundary layer developing spatially over a flat plate. *J. Fluid Mech.,* **326,** 1–37.

Durran, D. R., 1986: Another look at downslope windstorms. Part I: The development of analogs to supercritical flow in an infinitely deep, continuously stratified fluid. *J. Atmos. Sci.,* **43,** 2527–2543.

Flamant, C., and Coauthors, 2002: Gap flow in an Alpine valley during a shallow south foehn event: Observations, numerical simulations and hydraulic analogue. *Quart. J. Roy. Meteor. Soc.,* **128,** 1173–1210.

Glasnovic, D., and V. Jurcec, 1990: Determination of upstream bora layer depth. *Meteor. Atmos. Phys.,* **43,** 137–144.

Gohm, A., and G. J. Mayr, 2004: Hydraulic aspect of foehn winds in an Alpine Valley. *Quart. J. Roy. Meteor. Soc.,* **130,** 449–480.

——, and ——, 2005: Numerical and observational case-study of a deep Adriatic bora. *Quart. J. Roy. Meteor. Soc.,* **131,** 1363–1392.

——, ——, A. Fix, and A. Giez, 2008: On the onset of bora and the formation of rotors and jumps near a mountain gap. *Quart. J. Roy. Meteor. Soc.,* **134,** 21–46.

Houghton, D. D., and A. Kasahara, 1968: Nonlinear shallow fluid flow over an isolated ridge. *Commun. Pure Appl. Math.,* **21,** 1–23.

Jiang, Q., and J. D. Doyle, 2008: Diurnal variation of downslope winds in Owens Valley during the Sierra Rotor Experiment. *Mon. Wea. Rev.,* **136,** 3760–3780.

——, ——, and R. B. Smith, 2006: Interaction between trapped waves and boundary layers. *J. Atmos. Sci.,* **63,** 617–633.

——, ——, S. Wang, and R. B. Smith, 2007: On boundary layer separation in the lee of mesoscale topography. *J. Atmos. Sci.,* **64,** 401–420.

Klemp, J. B., and D. K. Lilly, 1975: The dynamics of wave induced downslope winds. *J. Atmos. Sci.,* **32,** 320–339.

——, and R. Wilhelmson, 1978: The simulation of three dimensional convective storm dynamics. *J. Atmos. Sci.,* **35,** 1070–1096.

——, and D. R. Durran, 1987: Numerical modelling of bora winds. *Meteor. Atmos. Phys.,* **36,** 215–227.

——, R. Rotunno, and W. C. Skamarock, 1997: On the propagation of internal bores. *J. Fluid Mech.,* **331,** 81–106.

Lamb, K. G., 1994: Numerical simulations of stratified inviscid flow over a smooth obstacle. *J. Fluid Mech.,* **260,** 1–22.

Lilly, D. K., and E. J. Zipser, 1972: The Front Range windstorm of January 11, 1972. *Weatherwise,* **25,** 56–63.

Lin, Y., and T. Wang, 1996: Flow regimes and transient dynamics of two-dimensional stratified flow over an isolated mountain ridge. *J. Atmos. Sci.,* **53,** 139–158.

Long, R. R., 1954: Some aspects of the flow of stratified fluids. Part II: Experiments with a two fluid system. *Tellus,* **6,** 97–115.

——, 1955: Some aspects of the flow of stratified fluids. Part III: Continuous density gradients. *Tellus,* **7,** 341–357.

Miller, D. M., W. A. R. Brinkmann, and R. G. Barry, 1974: Windstorms: A case study of wind hazards for Boulder, Colorado. *Natural Hazards: Local, National, Global,* G. F. White, Ed., Oxford University Press, 80–86.

Mobbs, S. D., and Coauthors, 2005: Observations of downslope winds and rotors in the Falkland Islands. *Quart. J. Roy. Meteor. Soc.,* **131,** 329–351.

Norte, F. A., 1988: Caracterìsticas del viento Zonda en la regìon de Cuyo. Ph.D. thesis, Buenos Aires University, 355 pp. [Available from Programa Regional de Meteorologìa, Instituto Argentino de Nivologìa, Glacialogìa y Ciencias Ambientales, Centro Regional de Investigaciones Cientificas y Teìcnicas (CRICYT)/ CONICET, Calle Bajada del Cerro s/n (5500) Mendoza, Argentina.]

Peltier, W. R., and T. L. Clark, 1979: The evolution and stability of finite-amplitude mountain waves. Part II: Surface wave drag and severe downslope windstorms. *J. Atmos. Sci.,* **36,** 1498–1529.

Seluchi, M. E., F. A. Norte, P. Satyamurty, and S. C. Chou, 2003: Analysis of three situations of the foehn effect over the Andes (Zonda wind) using the Eta-CPTEC regional model. *Wea. Forecasting,* **18,** 481–501.

Skyllingstad, E. D., 2003: Large eddy simulation of katabatic flows. *Bound.-Layer Meteor.,* **106,** 217–243.

——, and H. W. Wijesekera, 2004: Large eddy simulation of flow over obstacles: High drag states and mixing. *J. Phys. Oceanogr.,* **34,** 94–112.

Smith, C. M., and E. D. Skyllingstad, 2005: Numerical simulation of katabatic flow with changing slope angle. *Mon. Wea. Rev.,* **133,** 3065–3080.

——, and ——, 2009: Investigation of upstream boundary layer influence on mountain wave breaking and lee-wave rotors using a large eddy simulation. *J. Atmos. Sci.,* **66,** 3147–3164.

Smith, R. B., 1985: On severe downslope winds. *J. Atmos. Sci.,* **42,** 2597–2603.

——, Q. Jiang, and J. Doyle, 2006: A theory of gravity wave absorption by a boundary layer. *J. Atmos. Sci.,* **63,** 774–781.

Steppeler, J., H.-W. Bitzer, M. Minotte, and L. Bonaventura, 2002: Nonhydrostatic atmospheric modeling using a z-coordinate representation. *Mon. Wea. Rev.,* **130,** 2143–2149.

Vosper, S. B., 2004: Inversion effects on mountain lee waves. *Quart. J. Roy. Meteor. Soc.,* **130,** 1723–1748.

Ying, Q., and F. Baopu, 1993: A theoretical study on the interaction between airflow over a mountain and the atmospheric boundary layer. *Bound.-Layer Meteor.,* **64,** 101–126.

Zhong, S., J. Li, C. B. Clements, S. F. J. De Wekker, and X. Bian, 2008: Forcing mechanism for the Washoe Zephyr. *J. Appl. Meteor. Climatol.,* **47,** 339–350.